Proceedings of the Canadian Society for Mechanical Engineering International Congress
32nd Annual Conference of the Computational Fluid Dynamics Society of Canada
Canadian Society of Rheology Symposium
CSME/CFDSC/CSR 2025
May 25–28, 2025, Montréal, Québec, Canada

NUMERICAL ANALYSIS OF BUOYANCY-DRIVEN IMMISCIBLE EXCHANGE FLOWS IN AXIALLY ROTATING PIPES

Wenjie Liu,[1] Hossein Rahmani,[2] Faïçal Larachi,[1] Seyed Mohammad Taghavi[1]*

[1]Department of Chemical Engineering, Université Laval, Québec, Canada
[2]Department of Mathematics, The University of British Columbia, Vancouver, Canada
*Seyed-Mohammad.Taghavi@gch.ulaval.ca

***Abstract*—**This numerical investigation examines buoyancy-driven immiscible exchange flows in near-horizontal rotating pipes using OpenFOAM simulations, with direct applications to primary cementing of oil and gas wells. The study analyzes a density-unstable configuration where a higher-density fluid (water solutions) overlies a lower-density fluid (silicone oil), focusing on three critical parameters: the pipe's rotational angular velocities, density differences between fluids, and inclination angles. Analysis reveals that the displacing front velocity is an increasing function of density differences and a decreasing function of inclination angles and rotations. Higher density differences, faster rotations, and steeper inclinations could all enhance the Kelvin–Helmholtz instability. Higher pipe rotation dampens axial velocity fluctuations while enhancing radial direction velocity fluctuations, whereas both increased density differences and decreased inclination angles intensify axial velocity fluctuations, with cross-sectional components remaining relatively unchanged across all conditions. Additionally, turbulent kinetic energy is enhanced by faster rotations, higher density differences, and steeper inclination angles. These findings characterize the complex interplay between rotation, density difference, and inclinations in immiscible exchange flows, and provide some insights into practical cementing operations through velocity fluctuation and turbulent kinetic energy analysis.

***Keywords*—OpenFOAM simulation; immiscible fluids; exchange flow; rotating pipe; velocity fluctuations; turbulent kinetic energy**

I. INTRODUCTION

In recent years, rotating liner cementing technology has been employed worldwide, necessitating the study of the displacement of cement under rotational conditions [1]. Compared to traditional cementing methods, rotating-while-cementing is particularly advantageous in several scenarios, such as high-angle and horizontal wells, long-extended wells, wells with multiple loss zones, and wells with poor centralization [2]. Field studies evaluating cement bond quality during rotating liner operations have demonstrated promising results: 90% of applications achieved satisfactory bond quality, with 30% exhibiting exceptional bonding characteristics [3]. Implementing rotating liner hanger cementing techniques has been shown to address complex drilling challenges. This approach effectively reduces liner running resistance while significantly enhancing cement slurry displacement efficiency during cementing operations [4]. Other related studies have highlighted several significant benefits of rotating-while-cementing techniques: they can reduce gas and mud channeling, ensure robust loss control, improve zonal isolation, and enhance long-term production performance [2, 5, 6]. A schematic of rotating-while-cementing procedures is shown in Fig. 1(a).

During primary cementing operations, density differences between the cement slurry and in-situ fluid can trigger gravity-driven exchange flows, which are particularly challenging in deviated and horizontal wellbores. This phenomenon can result in fluid stratification when displacement efficiency decreases, creating a fallback effect that compromises cement sheath integrity through void formation and mechanical weak points[7, 8]. Such exchange flows are especially problematic during periods of low pumping rates or operational pauses caused by equipment failures or operational constraints. To maintain wellbore integrity, engineers must anticipate and manage fluid redistribution by carefully controlling density differences and flow rates throughout the cementing process.

Buoyant-driven miscible exchange flows have emphasized the effects of pipe inclination and density contrast on flow behavior [9]. Eslami *et al.* [10] demonstrated that the degree of flow instability and mixing enhances as the pipe is progressively inclined towards vertical. The maximal rate of fluid interpenetration occurs at an intermediate angle. Suckale *et*

The Canada Research Chair in Modeling Complex Flows (Grant No. CG125810); The Natural Sciences and Engineering Research Council of Canada (Grant No. CG10915); The National Scholarship Fund from CSC (Grant No. 202008320355).

al. [11] identified the inherent instability of two distinct stable flow patterns: core-annular flow and side-by-side flow. Investigations of unconfined 3-dimensional gravity currents using the lock exchange mechanism and large eddy simulations revealed three regimes: slumping, inertial–buoyancy equilibrium, and viscous–buoyancy equilibrium [12].

Immiscible buoyant exchange flows, where two fluids of different densities do not mix, represent a significant knowledge gap in fluid mechanics research, despite their critical importance in various industrial applications such as oil and gas well cementing, geological CO_2 sequestration, and chemical processing. The behavior of an elastic-viscoplastic fluid placed in silicone oil within vertical pipes was investigated in [13]. Rayleigh-Taylor, diffusive layer convection, and Rayleigh-Bénard instabilities were observed in buoyant exchange flows in [14]. Furthermore, the front velocity of the displacing fluid was characterized in inclined and horizontal configurations of immiscible exchange flows in [15].

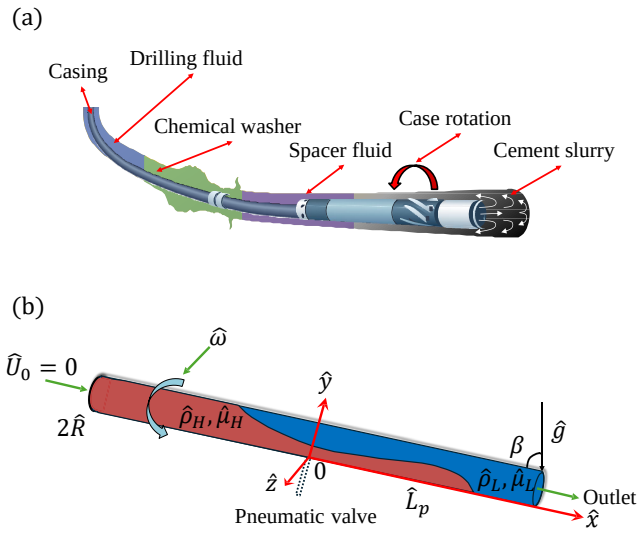

Figure 1. (a) The rotating-while-cementing procedure consists of the following sequential steps: imposing a chemical washer, pumping spacer fluid, placing cement slurry during pipe rotation, and pumping displacement fluid to maintain pressure balance. (b) Schematic of the simulation setup for the exchange flow system: an inclined pipe at angle β rotates at speed $\hat{\omega}$ along its axis. Imposed flow velocity $\hat{U}_0 = 0$ and outlet are indicated by arrows. The pipe contains displacing fluid (viscosity $\hat{\mu}_H$, density $\hat{\rho}_H$) and displaced fluid (viscosity $\hat{\mu}_L$, density $\hat{\rho}_L$) in red and blue regions, respectively. The arrow $\hat{g}$ indicates the gravitational direction. Coordinates ($\hat{x}$, $\hat{y}$) originate at the gate valve, measured from the bottom of the pipe.

Previous studies have conducted limited investigations into the effects of rotation on displacement flows. Lyu *et al.* [16], [17] explored these effects in a miscible configuration, while the immiscible configuration was studied in [18]–[20]. Additional research examined miscible exchange flow in a rotating pipe in [21]. These investigations considered multiple factors, including imposed flow inertia, tangential forces from rotation, the behavior of Newtonian and yield stress fluids, buoyant forces, and the effects of pipe inclination. However, immiscible exchange flows in axially rotating pipes remain largely unexplored in the literature.

The lack of statistical analysis of turbulent characteristics in buoyancy-driven immiscible exchange flows also provides the primary motivation for this study. Previous research has made several contributions, i.e., three-dimensional simulations of fully turbulent lock-exchange gravity currents have examined fluctuation velocity and turbulent kinetic energy budgets [22], while other studies have evaluated potential energy, kinetic energy, and dissipation in lock-exchange flows [23]. Additionally, Ottolenghi *et al.* [24] have investigated lock-release gravity currents flow up slopes.

Our present analysis of immiscible exchange flows is based on numerical investigation using OpenFOAM simulations. The study examines a density-unstable stratification where a higher-density fluid positioned above a lower-density fluid drives gravitational exchange flows, focusing on three critical parameters: pipe's rotational angular velocities, density differences between fluids, and inclination angles on velocity fluctuations, and turbulent kinetic energy. The paper is organized into the following main sections: Section II illustrates the research methodology, including problem formulation, simulation methods, and computational analysis methods. Section III examines immiscible exchange flows by presenting concentration and velocity field results, and then by analyzing the flow characteristics including velocity fluctuations, and turbulent kinetic energy. Section IV provides a brief conclusion.

II. Methodology

A. Problem Formulation

The exchange flow conditions exist in the primary cementing process as illustrated in Section I. This study investigates immiscible exchange flows in an inclined rotating pipe. The simulation setup (as shown in Fig. 1(b)) consists of a pipe of radius $\hat{R}$ and length $\hat{L}_p$ oriented at angle β from vertical. The pipe contains equal volumes of displacing (upper, $\hat{\rho}_H$, $\hat{\mu}_H$) and displaced (lower, $\hat{\rho}_L$, $\hat{\mu}_L$) fluids, with open boundary conditions at both ends. The pipe rotates with an angular velocity $\hat{\omega}$ along its axis, with zero imposed velocity for the displacing fluid. The initial fluid interface aligns with the pneumatic valve's movement direction, and the valve opening initiates simultaneously with the pipe rotation and the exchange flow. The dimensional parameters are presented in TAB. I. TAB. II lists the relevant dimensionless parameters.

TABLE I
THE IMMISCIBLE EXCHANGE FLOW DIMENSIONAL PARAMETERS IN OUR SIMULATIONS, INSPIRED BY TYPICAL EXPERIMENTAL VALUES.

Parameters	Symbols	Value or ranges [Unit]
Pipe's length	$\hat{L}_p$	1.4 [m]
Pipe's radius	$\hat{R}$	0.00952 [m]
Imposed flow	$\hat{U}_0$	0 [m s^{-1}]
Density	$\hat{\rho}_H$, $\hat{\rho}_L$	998, 918 [kg s^{-3}]
Viscosity	$\hat{\mu}_H$, $\hat{\mu}_L$	[1,4]×10^{-3} [Pa s^{-1}]
Interfacial tension	$\hat{\sigma}$	0.035 [N m^{-1}]
Angular velocity	$\hat{\omega}$	0-60 [rad s^{-1}]

TABLE II
THE IMMISCIBLE EXCHANGE FLOW DIMENSIONLESS PARAMETERS.

Parameters	Symbols or Formula	Value or ranges
Inclinations	β	60°, 75°, 83°
Pipe's length	$L = \frac{\hat{L}_p}{\hat{R}}$	147
Atwood number	$At = \frac{\hat{\rho}_H - \hat{\rho}_L}{\hat{\rho}_H + \hat{\rho}_L}$	0.04, 0.06, 0.08
Viscosity ratio	$M = \frac{\hat{\mu}_H}{\hat{\mu}_L}$	0.25
Buoyancy/tangential forces	$\frac{Fr}{Rb} = \frac{\hat{\omega}\hat{R}}{\hat{U}_i}$ *	$0 - 0.98$

* Buoyancy-inertial velocity: $\hat{U}_i = \sqrt{At\hat{g}\hat{R}}$.

Analysis of dimensionless parameters reveals two key driving factors: buoyancy-driven and rotational tangential forces. The buoyant force, affected by pipe angle and Atwood number (density difference), dominates the flow patterns. The Froude over Rossby number ($Fr/Rb \sim$[0,0.98]) quantifies the balance between buoyancy-driven and rotational tangential forces.

B. Solution Methods

This study uses transient simulations with assumptions of incompressible, isothermal, and immiscible fluids. The interface between heavy and light fluids is tracked using the volume of fluid (VOF) method via OpenFOAM's *interFoam* solver (based on Galilean reference frame). It solves the following set of continuity and momentum balance equations, respectively:

$$\boldsymbol{\nabla} \cdot \hat{\boldsymbol{U}} = 0, \tag{1}$$

$$\begin{aligned} \frac{\partial}{\partial \hat{t}}(\hat{\rho}\hat{\boldsymbol{U}}) + \nabla \cdot (\hat{\rho}\hat{\boldsymbol{U}}\hat{\boldsymbol{U}}) = -\nabla \hat{P}_d^* + \hat{\boldsymbol{x}} \cdot \hat{\boldsymbol{g}} \nabla \hat{\rho} \\ + \nabla \cdot \hat{\boldsymbol{\tau}} + \hat{\boldsymbol{F}}_\sigma, \end{aligned} \tag{2}$$

subjected to the rotating speed $\hat{\omega}$ of the pipe and the imposed flow velocity $\hat{U}_0 = 0$. The volume of fraction α_H is modeled by the following advection equation:

$$\frac{\partial \alpha_H}{\partial \hat{t}} + \nabla \cdot (\alpha_H \hat{\boldsymbol{U}}) + \nabla \cdot ((1 - \alpha_H)\alpha_H \hat{\boldsymbol{U}}_c) = 0. \tag{3}$$

In the above equations, $\hat{\rho}$ is the density, $\hat{\boldsymbol{U}}$ is the velocity vector, $\hat{\boldsymbol{U}}_c$ is a relative velocity that acts as a velocity perpendicular to the interface, $\hat{t}$ is the time, $\hat{\boldsymbol{g}}$ represents the gravitational acceleration, $\hat{\boldsymbol{x}}$ is the position vector, $\hat{P}_d^*$ calculated by subtracting the hydrostatic pressure from the static pressure ($\hat{P}_d^* = \hat{P}^* - \hat{\rho}\hat{\boldsymbol{g}} \cdot \hat{\boldsymbol{x}}$), $\hat{\boldsymbol{\tau}}$ denotes the shear stress tensor, and $\hat{\boldsymbol{F}}_\sigma$ is the source of momentum due to the interfacial tension.

A mesh independence study using three resolutions (coarse: 1,240,000 cells, medium: 1,360,000 cells, fine: 1,480,000 cells) led to selecting the medium mesh for optimal accuracy-efficiency balance, with front position deviations within 5.5% across resolutions. Numerical predictions showed good agreement with experimental data (front position deviations $< 6\%$). The simulation framework employs VOF method for interface tracking, with Gauss linear (gradients), GaussLimitedLinearUpwind (velocity flux), and Gauss VanLeer (phase fractions) discretization schemes. The PIMPLE algorithm with explicit Euler temporal discretization and adaptive time-stepping (max Courant: 0.2) manages pressure-velocity coupling, while parallel computations run on 40 cores (500 MB/CPU) using Calcul Québec and Digital Research Alliance of Canada clusters. Domain decomposition and reconstruction are managed using OpenFOAM's decomposePar and reconstructPar utilities. The setup consists of a pipe with the following boundary conditions: a zero-flow inlet, a constant pressure outlet. The pipe wall is subject to a no-slip condition and rotates at a defined angular velocity, as illustrated in Fig. 1(b).

C. Computational Analysis Methods

The mean velocity at each spatial direction is shown as:

$$\bar{\hat{U}}_i = \frac{1}{N} \sum_{n=1}^{N} \hat{U}_i \tag{4}$$

In the equation, N represents the number of velocity components in each direction. i indicates x, y, and z in three spatial directions. $\hat{U}_i$ refers to the velocity at the node. The velocity fluctuation is calculated as the difference between node velocity and mean velocity, expressed as:

$$\hat{U}_i' = \hat{U}_i - \bar{\hat{U}}_i \tag{5}$$

The velocity fluctuation indicates how much the local velocity varies from the average value of velocity [24]. Then the root mean square (RMS) of velocity fluctuations could be evaluated by:

$$\bar{\hat{U}}_{i:\mathrm{RMS}} = \sqrt{\frac{1}{N} \sum_{n=1}^{N} (\hat{U}_i')^2} \tag{6}$$

The turbulent kinetic energy (TKE) represents the mean kinetic energy per unit mass contained in the turbulent fluctuations, with higher TKE means more energetic turbulence [23]. To calculate the local TKE across the entire domain, each node along the center plane's axial direction is evaluated using:

$$\hat{k} = \frac{1}{2}((\hat{U}_x')^2 + (\hat{U}_y')^2 + (\hat{U}_z')^2) \tag{7}$$

Finally, the average turbulent kinetic energy (mTKE) for all domain is calculated by:

$$\bar{\hat{k}} = \frac{1}{2}(\bar{\hat{U}}_{x:\mathrm{RMS}}^2 + \bar{\hat{U}}_{y:\mathrm{RMS}}^2 + \bar{\hat{U}}_{z:\mathrm{RMS}}^2) \tag{8}$$

III. RESULTS

Section III-A presents concentration images and velocity fields along the pipe's center-plane (xy direction), while Section III-B analyzes velocity fluctuations and turbulent kinetic energy. Velocities are nondimensionalized using the buoyancy-inertial velocity scale $\hat{U}_i = \sqrt{At\hat{g}\hat{R}}$, with lengths scaled by $\hat{R}$, times by $\hat{R}/\hat{U}_i$, and turbulent kinetic energy by $\hat{U}_i^2$.

A. General Flow Observations

The image sequences in Fig. 2 illustrate the concentration (Cn) evolution of immiscible exchange flows along the pipe's center plane under varying rotational (Fr/Rb), density difference (At), and inclination (β) parameters. It provides optimal visualization, as the interface remains clearly defined. Cases (a) and (b) share the identical Atwood number ($At = 0.08$) and inclination angle ($\beta = 83°$), but differ in their rotational parameter Fr/Rb. In case (a) [$Fr/Rb = 0$], the wave number increases with time, characterized by both large amplitude waves and fast waves throughout the flow domain. In contrast, case (b) [$Fr/Rb = 0.69$] exhibits damped interfacial waves under rotation, evidenced by longer wave periods and reduced amplitudes. Meanwhile, in the static case, the displacing front moves faster, taking less time to pass through the pipe. Cases (b) and (c) have identical inclination angle and angular velocity but different Atwood numbers. Case (b), with higher At, exhibits more waves with pronounced tail fluctuations. In case (c), with lower At, the wave number is smaller compared to case (b), where the wavelengths are larger and the large wave numbers are damped, leading to a reduction of tail fluctuations. Finally, the inclinations could be compared in case (b) and case (d). The lower inclination in case (d) produces stronger interfacial instabilities than in case (b).

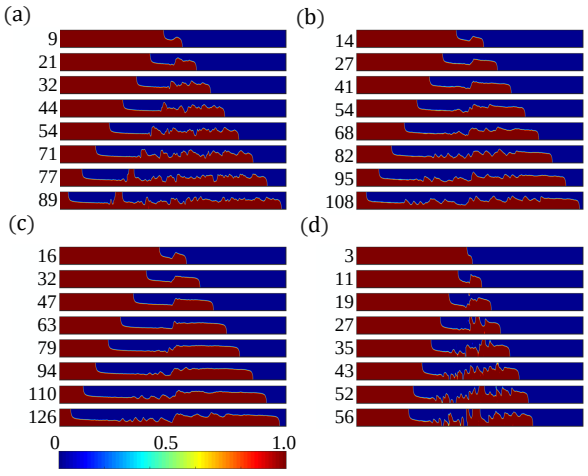

Figure 2. Image sequences of concentration (Cn) for immiscible exchange flows from the pipe's center plane ($x - y$ direction): (a) $Fr/Rb = 0$, $At = 0.08$, and $\beta = 83°$. (b) $Fr/Rb = 0.69$, $At = 0.08$, and $\beta = 83°$. (c) $Fr/Rb = 0.80$, $At = 0.06$, and $\beta = 83°$. (d) $Fr/Rb = 0.69$, $At = 0.08$, and $\beta = 60°$. Dimensionless time (t) is presented on the left of each snapshot. The field of view is 2×147 (dimensionless pipe diameter × dimensionless length); and the below color bar shows the normalized concentration (0: displaced fluid; 1: displacing fluid).

Figure 3 presents image sequences of axial velocities (U_x) for immiscible flows in the center plane of a pipe under varying conditions. The velocity field is normalized and visualized through a color map ranging from -2.5 (blue, indicating downward flow) to 2.5 (red, indicating upward flow), with green representing zero-velocity regions. Cases (a) through (d) correspond to different combinations of the rotating parameter

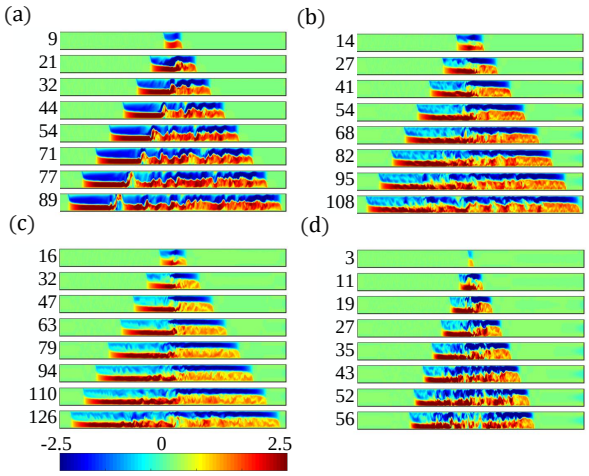

Figure 3. Image sequences of axial velocities (U_x) for immiscible exchange flows from the pipe's center plane ($x - y$ direction). From (a) to (d), the parameters are the same as in Figure 2. The below color bar shows the range of normalized axial velocity.

(Fr/Rb), Atwood number (At), and angle of inclination (β). The velocity fields reveal distinct flow characteristics. The stationary case (a) shows strong velocity gradients near the interface ($t = 9 - 89$). The rotating case (b) exhibits scattered and non-uniform velocity structures ($t = 14 - 108$), particularly in the displaced fluid tail. Case (c), with a lower density difference compared to case (b), extends over a longer duration ($t = 16 - 126$), due to the smaller axial velocities. Case (d), with lower inclination, shows intensified velocity fluctuations in shorter duration ($t = 3 - 56$). These velocity distributions correspond directly to the interfacial instability patterns observed in the concentration fields (Fig. 2).

B. Flow Characteristic Analysis

Figure 4 illustrates the RMS velocity fluctuations under different flow conditions. When comparing cases (a_1) and (a_2) at constant $At = 0.04$ and $\beta = 83°$, the introduction of rotation (Fr/Rb from 0 to 0.98) significantly alters the velocity fluctuations. In the stationary case (a_1), the axial direction component $\overline{U}_{x:\mathrm{RMS}}$ increases monotonically from 0.2 to 0.6, while in the rotating case (a_2), $\overline{U}_{x:\mathrm{RMS}}$ approximately reaches a maximum value of 0.4. In the cross-section, the vertical direction velocity fluctuation component $\overline{U}_{y:\mathrm{RMS}}$ remains below 0.2 in both cases, but in the rotating case, the z direction velocity fluctuation component $\overline{U}_{z:\mathrm{RMS}}$ peaks at approximately 0.5 around $t = 100$ before declining to 0.4, and the value is larger than in the stationary case. These findings offer a distinctive insight into how rotation influences turbulent characteristics in immiscible exchange flows. Rotation effectively suppresses axial velocity fluctuations while enhancing transverse fluctuations, effectively redistributing turbulent kinetic energy from the axial direction to the transverse direction.

The cases (b_1 and b_2) exhibit higher density ratios (Atwood number, At) compared to cases (a_1 and a_2), while all cases

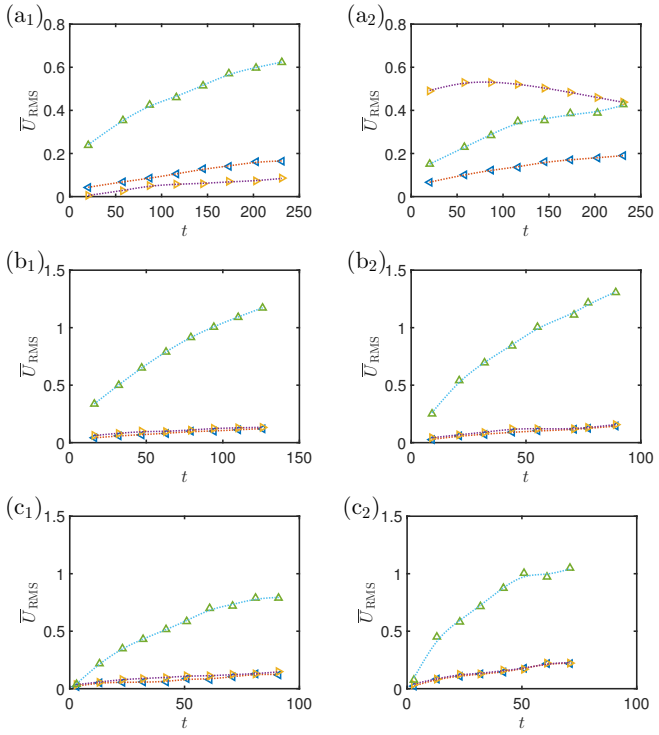

Figure 4. Comparison of root mean square (RMS) of velocity fluctuations ($\overline{U}_{\mathrm{RMS}}$) versus time ($t$). Symbols represent: $\overline{U}_{z:\mathrm{RMS}}$ (▷), $\overline{U}_{y:\mathrm{RMS}}$ (◁), $\overline{U}_{x:\mathrm{RMS}}$ (△), and overall RMS of velocity fluctuations $\overline{U}_{\mathrm{RMS}}$ (◯), in each separate panel: (a_1) $Fr/Rb = 0$, $At = 0.04$, and $\beta = 83°$. (a_2) $Fr/Rb = 0.98$, $At = 0.04$, and $\beta = 83°$. (b_1) $Fr/Rb = 0.16$, $At = 0.06$, and $\beta = 83°$. (b_2) $Fr/Rb = 0.16$, $At = 0.08$, and $\beta = 83°$. (c_1) $Fr/Rb = 0.16$, $At = 0.04$, and $\beta = 75°$. (c_2) $Fr/Rb = 0.16$, $At = 0.04$, and $\beta = 60°$.

maintain the same angle of $\beta = 83°$ and rotating of $Fr/Rb = 0.16$. The axial component velocity fluctuations $\overline{U}_{x:\mathrm{RMS}}$ increase with higher density differences. At At=0.08, axial direction velocity fluctuations reaches $\overline{U}_{x:\mathrm{RMS}}$=1.3. However, the cross-section components ($\overline{U}_{y:\mathrm{RMS}}$ and $\overline{U}_{z:\mathrm{RMS}}$) remain below 0.2, demonstrating minimal sensitivity to density differences under a moderate rotation. Finally, the reduction in inclination angle from $\beta = 75°$ (case c_1) to $\beta = 60°$ (case c_2) significantly affects velocity fluctuations. The vertical component ($\overline{U}_{x:\mathrm{RMS}}$) shows faster growth and reaches a higher magnitude (~ 1.0) in case (c_2) compared to case (c_1) (~ 0.8). Both cases maintain similar cross-sectional fluctuations ($\overline{U}_{y:\mathrm{RMS}}$ and $\overline{U}_{z:\mathrm{RMS}}$), below 0.3, indicating that inclination angle primarily influences the axial direction velocity fluctuations while having minimal impact on cross-section components.

Figure 5 presents image sequences of normalized turbulent kinetic energy (TKE, k) in immiscible exchange flows observed from the center plane of the pipe. The visualization compares four scenarios with varying Froude number ratios (Fr/Rb) and inclination angles (β). Comparing scenarios (a) and (b), the introduction of rotation effects ($Fr/Rb = 0.98$) leads to increased turbulence at near wall boundaries and more fragmented flow patterns compared to the non-rotating case ($Fr/Rb = 0$). The influence of inclination angle becomes

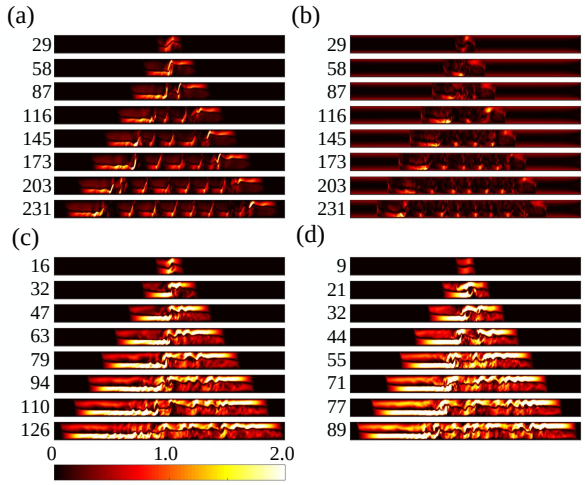

Figure 5. Image sequences of the normalized turbulent kinetic energy (TKE, k) for immiscible exchange flows from the pipe's center plane ($x - y$ direction): (a) $Fr/Rb = 0$, $At = 0.04$, and $\beta = 83°$. (b) $Fr/Rb = 0.98$, $At = 0.04$, and $\beta = 83°$. (c) $Fr/Rb = 0.12 \pm 0.01$, $At = 0.04$, and $\beta = 75°$. (d) $Fr/Rb = 0.12 \pm 0.01$, $At = 0.04$, and $\beta = 60°$. Dimensionless time (t) is presented on the left of each snapshot. The below color bar ranges from 0 to 2, with dark indicating lower turbulent kinetic energy levels and bright showing higher turbulent kinetic energy intensities.

apparent when examining scenarios (c) and (d). At a lower angle ($\beta = 60°$), Scenario (d) exhibits more concentrated energy patterns, indicated by intense and pronounced color gradients, developing over a shorter duration (t=9 to 89). In contrast, scenario (c) at $\beta = 75°$ displays more elongated structures that evolve over an extended period (t=16 to 126). Additionally, the comparison between scenarios (b) and (c) reveals that reducing the inclination angle from $\beta = 83°$ to $\beta = 75°$ results in more pronounced turbulent structures.

Figure 6 provides a comprehensive analysis of the temporal evolution (t) of average-normalized turbulent kinetic energy ($\bar{k}$) under different flow conditions. In case (a), at constant Atwood number (At=0.04) and inclination ($\beta = 83°$), the introduction of rotation (Fr/Rb=0.98) accelerates mTKE development compared to stationary flow (Fr/Rb=0), reaching $\bar{k} \approx 0.2$ at t=100, highlighting rotation's enhancement of turbulence. Case (b) demonstrates that at higher density difference (At=0.08) and same inclination ($\beta = 83°$), increasing rotating speed from Fr/Rb=0.05 to 0.35 enhances mTKE growth significantly, achieving $\bar{k} \approx 0.7$ by t=100, indicating that higher rotation speeds lead to more rapid mTKE growth. In case (c), the higher density difference (At=0.08 vs 0.06) leads to more rapid mTKE development, reaching $\bar{k} \approx 0.9$ at t=100. Finally, case (d) reveals that at constant rotation (Fr/Rb=0.12) and density difference (At=0.04), reducing inclination from $\beta = 75°$ to $\beta = 60°$ substantially enhances mTKE, with the lower angle achieving $\bar{k} \approx 0.6$ compared to $\bar{k} \approx 0.3$, demonstrating inclination's strong influence on the turbulent energy.

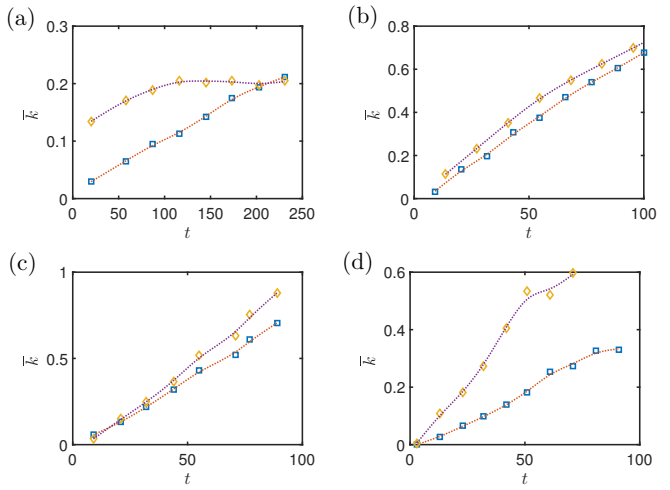

Figure 6. Comparisons of average-normalized turbulent kinetic energy (mTKE, $\bar{k}$) versus time (t). (a) Comparisons of stationary and rotating exchange flows at $At = 0.04$, and $\beta = 83°$, symbols represent: $Fr/Rb = 0$ (□), $Fr/Rb = 0.98$ (◇). (b) Comparisons of rotating effects at $At = 0.08$, and $\beta = 83°$, $Fr/Rb = 0.05$ (□), $Fr/Rb = 0.35$ (◇). (c) Comparison of density differences at $\beta = 83°$, and $Fr/Rb = 0.12 \pm 0.01$, $At = 0.06$ (□), $At = 0.08$ (◇). (d) Comparisons of pipe's inclinations at $Fr/Rb = 0.12$ and $At = 0.04$, $\beta = 75°$ (□), $\beta = 60°$(◇).

IV. Conclusion

The present numerical investigation of immiscible exchange flows in inclined rotating pipes has revealed several significant findings with direct implications for rotating-while-cementing operations. The study demonstrates that pipe rotation (Fr/Rb up to 0.98) can enhance transverse velocity fluctuations and turbulent kinetic energy in the axial direction. Increased density differences (At from 0.06 to 0.08) accelerate the growth of turbulent kinetic energy and lead to more pronounced tail fluctuations, with axial velocity fluctuations reaching $\overline{U}_{x:\mathrm{RMS}}$=1.3 at At=0.08. Lower inclination angles (β from 75° to 60°) substantially enhance turbulent kinetic energy and produce stronger interfacial instabilities, primarily affecting axial velocity fluctuations while minimally impacting cross-sectional components. These results provide fundamental insights into the complex dynamics of immiscible exchange flows under rotation, advancing our understanding of the physical mechanisms involved and offering practical guidance for cementing operations in oil and gas wells.

Acknowledgment

This research was conducted at Université Laval through the Canada Research Chair in Modeling Complex Flows, with financial support provided by the Natural Sciences and Engineering Research Council of Canada (NSERC) and the Chinese Scholarship Council. Computations were provided by Calcul Québec and the Digital Research Alliance of Canada.

References

[1] X. Yang, J. Zhou, and J. Liu, "Numerical Simulation of Cementing Displacement Efficiency of Rotating Liner," IFEDC 2023, Springer Series in Geomechanics and Geoengineering, pp. 82–93, 2024.

[2] Al-Baiyat, M. Khalil, T. Heinold, and D. Porter, "Production liner cementing practices in challenging horizontal wellbores," Int. Petro. Tech. Conf. (IPTC), p. D011S014R002, 2019.

[3] A. Wilson, "Investigating the benefits of Rotating-Liner cementing and impact factors," J. Pet. Technol., vol. 69, no. 05, pp. 82–84, 2017.

[4] L. Ma, D. Wang, Z. Guo, C. Ruan, and L. Gu,"Research and practice of rotating technique for liner hanger," Open Pet. Eng. J., vol. 5, no. 1, pp. 88–97, Aug. 2012.

[5] W. Cai, J. Deng, M. Luo, Y. Feng, J. Li, and Q. Liu, "Recent advances of cementing technologies for ultra-HTHP formations," Int. J. Oil, Gas Coal Technol., vol. 29, no. 1, p. 27, 2021.

[6] W. W. Fleckenstein, A. W. Eustes, G. H. Yaakob, and R. D. Rostad, "Investigation of methods to rotate casing sections independent of surface rotation," Proc. SPE Annu. Tech. Conf. Exhib., p. D021S023R006, 2016.

[7] I. A. Frigaard, and J. P. Crawshaw, "Preventing buoyancy driven flows of two Bingham fluids in a closed pipe–Fluid rheology design for oilfield plug cementing." J. Eng. Math. Vol. 36 No. 4, pp. 327–348, 1999.

[8] S. Pelipenko and I. A. Frigaard, "Mud removal and cement placement during primary cementing of an oil well – Part 2; steady-state displacements," J. Eng. Math., vol. 48, no. 1, pp. 1–26, 2004.

[9] T. Séon, J.-P. Hulin, D. Salin, B. Perrin, and E. J. Hinch, "Buoyant mixing of miscible fluids in tilted tubes," Phys. Fluids, vol. 16, no. 12, pp. L103–L106, 2004.

[10] B. Eslami, S. Shariatnia, H. Ghasemi, and K. Alba, "Non-isothermal buoyancy-driven exchange flows in inclined pipes," Phys. Fluids, vol. 29, no. 6, p. 062108, 2017.

[11] J. Suckale, Z. Qin, D. Picchi, T. Keller, and I. Battiato, "Bistability of buoyancy-driven exchange flows in vertical tubes," J. Fluid Mech., vol. 850, pp. 525–550, Jul. 2018.

[12] R. Inghilesi, C. Adduce, V. Lombardi, F. Roman, and V. Armenio, "Axisymmetric three-dimensional gravity currents generated by lock exchange," J. Fluid Mech., vol. 851, pp. 507–544, Jul. 2018.

[13] P. R. Varges, B. S. Fonseca, C. M. Costa, M. F. Naccache, P. R. de Souza Mendes, and H. A. Pinho, "Exchange flows between yield stress materials and Newtonian oils," J. Non-Newtonian Fluid Mech., vol. 261, pp. 123–135, Nov. 2018.

[14] B. Taghiloo, P. Sadeghi, P. Sarmadi, M. Saffaripour, and K. Sadeghy, "Buoyancy-driven exchange flow of immiscible yield-stress fluids in a vertical closed-ended container," J. Non-Newtonian Fluid Mech., vol. 265, pp. 79–91, 2019.

[15] M. Yavari, M. Bazargan, N. Kazemi, E. Bagherizadeh, and J. Estevade-ordal, "Front dynamics in exchange flow of two immiscible iso-viscous fluids in two-dimensional straight and curved plane channels," Phys. Fluids, vol. 31, no. 9, p. 092105, 2019.

[16] S. Lyu and S. M. Taghavi. Stratified flows in axially rotating pipes. Phys. Rev. Fluids, vol. 3, no. 7, p. 074003, 2018.

[17] S. Lyu and S. M. Taghavi. Viscoplastic displacements in axially rotating pipes. J. Non-Newtonian Fluid Mech., vol. 284, p. 104353, 2020.

[18] W. Liu, H. Hassanzadeh, F. Larachi, and S. M. Taghavi, "Immiscible displacement flows in axially rotating pipes," Phys. Fluids, vol. 35, no.7, p. 072104, 2023.

[19] W. Liu, F. Larachi, and S. M. Taghavi, "Immiscible non-Newtonian displacement flows in stationary and axially rotating pipes," Phys. Fluids, Vol. 36, No. 10, p.102104, 2024.

[20] W. Liu, H. Rahmani, F. Larachi, and S. M. Taghavi, "Numerical simulation of immiscible Newtonian displacements in axially rotating pipes." Prog. Can. Mech. Eng., Conf. Proc. Vol. 7 No. 122, pp. 1–6, 2024.

[21] S. Lyu, M. Izadi, and S. M. Taghavi, "Exchange flows in axially rotating pipes," Phys. Rev. Fluids, vol. v5, no. 7, p. 074801, 2020.

[22] J. Pelmard, S. Norris, and H. Friedrich, "Statistical characterisation of turbulence for an unsteady gravity current," J. Fluid Mech., vol. 901, p. A7, 2020.

[23] S. K. Ooi, G. Constantinescu, and L. Weber, "Numerical simulations of lock-exchange compositional gravity current," J. Fluid Mech., vol. 635, pp. 361–388, 2009.

[24] L. Ottolenghi, C. Adduce, F. Roman, and V. Armenio, "Analysis of the flow in gravity currents propagating up a slope," Ocean Model (Oxf), vol. 115, pp. 1–13, 2017.